Optimization of a High Frequency Current Transformer sensor for Partial Discharge Detection using Finite Element Analysis

Christos Zachariades, Roger Shuttleworth, *Member, IEEE,* Riccardo Giussani, *Member, IEEE,* Ross MacKinlay

***Abstract*— High Frequency Current Transformer (HFCT) sensors are widely used for Partial Discharge detection due to their versatility, high sensitivity and wide bandwidth. This paper reports on a Finite Element Analysis (FEA) methodology that can be employed to optimize HFCT performance. The FEA model consists of accurate 3D representations of the sensor components. Two different FEA software modules were used in order to cover the wide operating frequency range of the sensor. The simulation computes the frequency response of the sensor in the range 0.3 MHz - 50 MHz for various HFCT geometric and material parameters, specifically the number of winding turns, spacer thickness, aperture size and core material. A prototype HFCT was constructed and the measured response compared with that of the simulation. The shapes of the responses were similar, with the simulated sensitivity being higher than the measured sensitivity by 1 dB on average. The measured low frequency cut-off of the sensor was found to be only 0.05 MHz lower than that of the simulation.**

***Index Terms*— condition monitoring, FEA, finite element analysis, frequency response, HFCT, high frequency current transformer, partial discharge, sensor.**

I. Introduction

Partial Discharge (PD) monitoring is a widely employed technique for diagnosing the condition of electrical insulation. It can be used to assess the condition of High Voltage plant assets including rotating machines, switchgear, transformers and cables [1]. Monitoring can be performed continuously or at regular intervals (spot-testing), while the asset is on-line or supplied from an external source, and can be combined with other monitoring methods to provide a holistic monitoring solution [2].

To detect PD, a variety of sensors can be used for different applications. These include High Voltage Coupling Capacitors, Rogowski Coils, Transient Earth Voltage detectors, Acoustic and RF sensors. One of the most versatile PD sensors is the High Frequency Current Transformer (HFCT). The HFCT usually consists of a wound, toroidal, ferrite core which is placed around an unscreened cable conductor or earth sheath to inductively detect PD [3]. The HFCT often has a split-core design, making it easy to install and suitable for retrofit installations. Also, HFCTs have good sensitivity and wide bandwidth making them ideal for remote monitoring [4].

When designing an inductive sensor, such as an HFCT, it is common to use equivalent circuits [5] or simplified models [6] to optimize its parameters. The aim of the study described here is to determine the suitability of Finite Element Analysis (FEA) in investigating the performance of a HFCT sensor. By using FEA, optimization of the sensor parameters can be performed in the virtual domain, avoiding the need for expensive and time consuming production of multiple prototypes. To achieve this, an accurate 3D simulation of a prototype sensor was constructed and the frequency response of the simulation examined as its various parameters were changed. The results from the simulation were compared with test results to determine the accuracy of the methodology. From this work an understanding of how the various HFCT parameters affect the response was gained.

II. Simulation Methodology

The performance of a HFCT sensor is primarily judged by how its sensitivity (transfer impedance) varies with frequency. The model described in the following sections was designed so that S-parameters can be computed. From the S-parameters the transfer impedance can then be derived. Additionally, the simulation closely resembles the arrangement used for testing the HFCT (*Section IV.A*). This allows straight forward comparison of experimental and simulated results.

A. Model

A three-dimensional model of the HFCT was initially assembled in Solidworks. For the metallic parts of the sensor, the existing 3D CAD models were used. The models for the core and spacers were created from the mechanical drawings of those parts. No dimensional approximations were made

Manuscript received June 27, 2016; revised August 11, 2016; accepted August 11, 2016. This work was co-funded by the UK's Innovation Agency, Innovate UK. Paper no. Sensors-15356-2016.

C. Zachariades is with the University of Manchester and High Voltage Partial Discharge Ltd, Salford, M50 2UW, UK (e-mail: christos@hvpd.co.uk).

R. Shuttleworth is with the University of Manchester (e-mail: roger.shuttleworth@manchester.ac.uk), Manchester, M13 9PL, UK.

R. Giussani (e-mail: riccardo.giussani@hvpd.co.uk) and R. Mackinlay are with High Voltage Partial Discharge Ltd, Salford, M50 2UW, UK.

Color versions of one or more of the figures in this paper are available online at http://ieeexplore.ieee.org.

Digital Object Identifier .

when simulating the insulated wire wrapped around the core. The wire had a radial insulation thickness of 0.3 mm and an overall diameter of 1.6 mm. Special care was taken to model the winding termination point as accurately as possible.

In order to reduce the number of elements required for the discretization, a few features of the casing were suppressed to simplify the model. These included the bolt holes, bolts, clasp, and other cosmetic recesses for the attachment of labels. The omission of these features should not affect the accuracy of the overall model since they are located on the external surfaces of the grounded metallic casing. The simplified 3D model of the sensor is shown in Fig. 1.

The Solidworks sensor model was imported into COMSOL Multiphysics where it was placed in the middle of a virtual box with dimensions 0.4 m × 0.4 m × 0.2 m (Fig. 2). The box serves a dual purpose. It defines the computation domain and its boundaries provide a low impedance return path for the current. The domain internally consists of air while its walls are defined to be lossless conducting boundaries in order to facilitate current conservation for the simulation. A vertical conductor passes through the center of the box and the HFCT. Where the conductor meets the upper and lower box surfaces, it meets the center conductors of two short coaxial cables, modelled as RG223. The screens of the two coaxial cables are electrically connected to the box. Another coaxial cable takes the signal from the BNC connector of the sensor to the nearest box boundary. The coaxial cables allow the implementation of boundary conditions required for model excitation and measurement of S-parameters (*Section II.C*).

B. Materials

The material properties required for the computation are the electrical conductivity, the relative permittivity and the relative permeability. These properties are shown in Table I.

Most of the material properties do not change significantly over the frequency range covered by the simulation. An exception however is the permeability of the ferrite core of the sensor. The relative magnetic permeability changes with frequency and plays an important part in the behavior of the sensor. To take into account the changing permeability, the real and imaginary permeability plots were sourced from the supplier. These unfortunately did not extend to the end of the required frequency range, stopping at 4 MHz, and so permeability plots from other studies were identified which show the permeability of the same ferrite material at higher frequencies [7]. The combined plots were digitized and imported into COMSOL where they were used to define interpolation functions of real and imaginary permeability against frequency (Fig. 3).

It is worth noting that the permittivity and conductivity of the ferrite also change with frequency [8] but the changes are relatively minor compared to the same properties of other

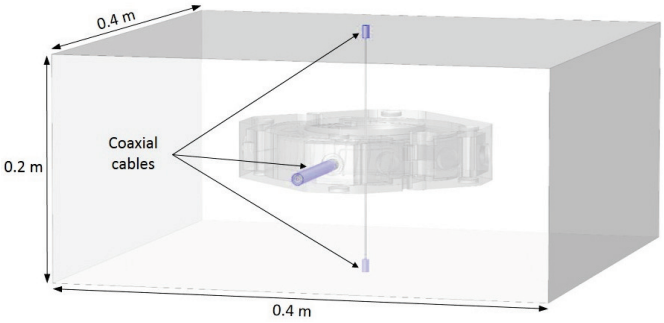

Fig. 2. Computation domain including the HFCT geometry. The outer boundaries of the domain provide a low impedance return path for the current. Short coaxial cables facilitate the excitation of the model.

TABLE I
MATERIAL PROPERTIES FOR COMPUTATION

Component	Material	Conductivity (S/m)	Relative permittivity	Relative permeability
Winding conductor	Copper	5.998×10^7	1.0	1.0
Winding insulation	PVC	0	3.0	1.0
Transmission line insulation	Polyethylene	0	2.4	1.0
Core	Ferrite	0	15.0	$\mu' - j\mu''$ **
Spacer	Nylon	0	4.0	1.0
Casing	Aluminium	3.774×10^7	1.0	1.0
Box	Air	0 - 0.01*	1.0	1.0

* The conductivity of air was increased to a small non-zero value for frequencies between 0.3 MHz and 0.6 MHz to speed convergence.

** μ' is the real and μ'' the imaginary permeability defined as interpolation functions.

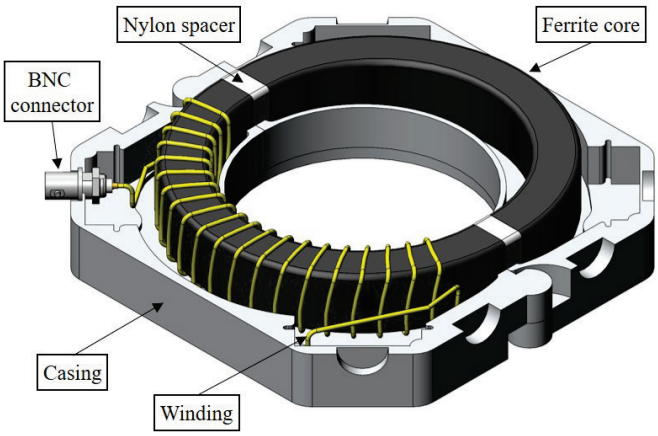

Fig. 1. HFCT model (20 winding turns) with the top part of the casing removed. The main components of the sensor are shown.

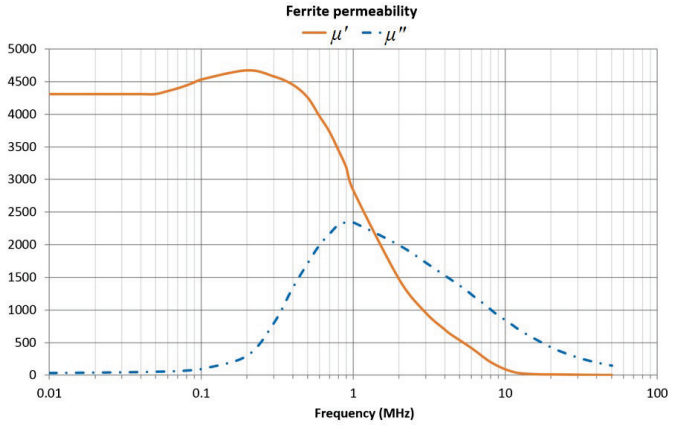

Fig. 3. Plots of real and imaginary ferrite permeability against frequency. The plots were digitized and imported into COMSOL Multiphysics where they were used to define interpolation functions that specify the behavior of the ferrite for the simulation.

materials in the model. It was therefore decided to treat these ferrite properties as being constant over the frequency range for simplicity.

C. Physics

COMSOL Multiphysics offers three modules that are appropriate for modelling at known frequencies, the AC/DC module, the RF module and the Wave Optics module. The decision on which of these modules to use depends mainly on the electrical size of the object being studied, the frequency and the memory limitations of the computing hardware. The frequency range of interest, between 0.3 MHz and 50 MHz, dictates that one of the AC/DC or RF modules should be used. COMSOL recommends using the AC/DC module when the characteristic length, L_c, of the object being analyzed is much smaller than the wavelength, λ, in free space:

$$L_c < \lambda/100 \tag{1}$$

Alternatively, the RF module should be used when the characteristic length is comparable to the wavelength [9]:

$$\lambda/100 < L_c < 10\lambda \tag{2}$$

The various dimensions of the HFCT parts and the frequencies of interest however, put the model at the boundary between the regions of applicability of the AC/DC and RF modules. Hence, it was decided to use the AC/DC module for frequencies between 0.3 MHz and 5 MHz and the RF module for frequencies between 5 MHz and 50 MHz.

For the lower end of the frequency range, the *Magnetic Fields* interface was used which solves a frequency-domain form of Ampere's Law for the magnetic and electric fields and the induced current:

$$\left(j\omega\sigma - \omega^2\varepsilon_0\right)\mathbf{A} + \nabla\times\left(\mu_0^{-1}\nabla\times\mathbf{A} - \mathbf{M}\right) = \mathbf{J}_e \tag{3}$$

where ω is angular frequency, σ is electrical conductivity, ε_0 and μ_0 are the permittivity and permeability of free space respectively, $\mathbf{A}$ is the magnetic vector potential, $\mathbf{M}$ is the magnetization of the material and $\mathbf{J_e}$ is the electric current density. For higher frequencies, the *Electromagnetic Waves* interface was used which solves a similar equation for the electric field, $\mathbf{E}$:

$$\nabla\times\left(\mu_r^{-1}\nabla\times\mathbf{E}\right) - \frac{\omega^2}{c_0^2}\left(\varepsilon_r - \frac{j\sigma}{\omega\varepsilon_0}\right)\mathbf{E} = 0 \tag{4}$$

where c_0 is the speed of light in vacuum, ε_r is relative permittivity, μ_r is relative permeability. The governing equations are formed assuming that the materials are linear isotropic i.e. the polarization depends linearly on the electric field and therefore the permittivity is constant.

At non-zero operating frequencies the current flowing in materials with finite conductivity is pushed towards the outer surface due to the skin effect. The effect becomes more pronounced as frequency increases and can be exploited to reduce the computation resources required to simulate the metallic domains of the model, such as the winding conductor and the casing. The saving in computation resources is achieved by assuming that the current flows only on the surface of the metallic objects of the model using the *Impedance Boundary Condition (IBC)*:

$$\sqrt{\frac{\mu_0\mu_r}{\varepsilon_0\varepsilon_r - j\dfrac{\sigma}{\omega}}}\,\hat{\mathbf{n}}\times\mathbf{H} + \mathbf{E} - \left(\mathbf{n}\cdot\mathbf{E}\right)\hat{\mathbf{n}} = 0 \tag{5}$$

where $\mathbf{H}$ is the magnetic field intensity and $\hat{\mathbf{n}}$ is the vector normal to the surface.

By using the *IBC* the interior of metallic domains can be excluded from the simulation i.e. it does not need to be discretized. When using the *IBC,* resistive losses due to the finite conductivity of the material can still be accurately computed providing the characteristic size, L_c, of the object is much larger than the skin depth, δ [10]:

$$L_c > 10\delta \tag{6}$$

The skin depth is defined as the distance from the surface over which the majority (≈ 63%) of the current is flowing [11]. As relatively low frequencies were used in the simulation, the permittivity of metals was considered to be unity and their permeability was considered to be real valued. Hence the skin depth becomes:

$$\delta = \sqrt{\frac{1}{\pi\cdot f\cdot\mu_0\cdot\sigma}} \tag{7}$$

where f is the frequency. The *IBC* was used on the casing of the HFCT and the winding conductor for frequencies above 5 MHz.

An additional constitutive relationship was added to the ferrite domain to account for magnetic losses. In essence the governing equations were modified to include a complex magnetic permeability in the form:

$$\mu_r = \mu' - j\mu'' \tag{8}$$

where μ' is the real and μ'' the imaginary permeability defined as interpolation functions (Fig. 3).

The outer boundaries of the computation domain and the shields of the coaxial cables were set to *Magnetic Insulation* (9) or *Perfect Electric Conductor (PEC)* (10) depending on the frequency. In both cases, they are considered to be lossless metallic surfaces, since the tangential components of magnetic

potential or electric field are set to zero:

$$\hat{\mathbf{n}} \times \mathbf{A} = 0 \quad (9)$$

$$\hat{\mathbf{n}} \times \mathbf{E} = 0 \quad (10)$$

Finally, the ends of the three coaxial cables were set to the *Coaxial Lumped Port Boundary Condition* which supports the calculation of S-parameters (Fig. 4). Excitation is specified in terms of voltage for Port 1 only. In other words, energy enters the model through Port 1 at the top of the computation domain and exits through Ports 2 and 3. All ports were 50 Ω terminated.

D. Discretization

When creating the geometric mesh a compromise must be made between the solution accuracy and the computational resource availability. As the number of elements increases the accuracy of the solution also increases but so does the memory required to solve the problem. Using a combination of knowledge regarding the geometric discretization error and engineering judgement the mesh can be refined to achieve a fast simulation with a high enough accuracy.

COMSOL by default uses second-order Lagrangian elements to discretize the geometry. An empirical rule of thumb is to use five such elements per wavelength [12-14]. Since the study examines the behavior of the sensor over a range of frequencies, the wavelength varies. Although it is possible to parametrize the mesh size based on frequency to reduce memory requirements, this was not applicable to this study. Other factors took precedence when deciding on optimum mesh size. This is because the shortest wavelength for the simulation at 50 MHz is 6 m which is much longer than the dimensions of any components in the model. For example, to ensure the quality of the mesh, at least two second-order elements were used per 90° arc [15] which, given the radii of the various components, are already much shorter than required. Also, the model contains components with large size differences which therefore need manual meshing for accurate representation.

Another parameter to be considered when discretizing the geometry is the skin depth, δ, defined in equation (7). If δ is comparable to the characteristic length of the object it is advised to use a boundary layer mesh to resolve the field variations inside a domain [12]. This type of mesh was used to discretize the winding conductor for frequencies below 5 MHz for when its interior is included in the simulation.

Part of the discretized geometry can be seen in Fig. 5 which shows that the mean density varies between parts. The most important mesh parameters are the following:

- Number of elements: 4.2 - 7.3 million
- Minimum element size: 0.12 mm
- Maximum element size: 12 mm

The number of elements varied between simulations because the dimensions of some parts were changed in order to investigate their effect on the frequency response of the sensor.

The simulations were performed on a workstation with an Intel® Xeon® E5-2667 v2 Processor (8 cores/16 threads) and 256 GB of DDR3 memory. The maximum total time taken to run the two simulations (AC/DC and RF) covering the entire frequency range was 17 hours and 45 minutes while memory utilisation reached 187 GB.

III. Simulation Results

Before proceeding to examine the frequency response of the sensor, it was necessary to check whether the simulation performs as intended. Fig. 6 shows the magnetic flux density plotted on a plane in the middle of the computation domain. The magnetic field lines, visualized as an arrow plot, form concentric circles around the current carrying wire. They have a clockwise direction since the current is flowing from the top of the model towards the bottom (into the page). The function of the ferrite core is also evident from Fig. 6. The low reluctance path provides efficient flux linkage between the current carrying wire and the sensor winding.

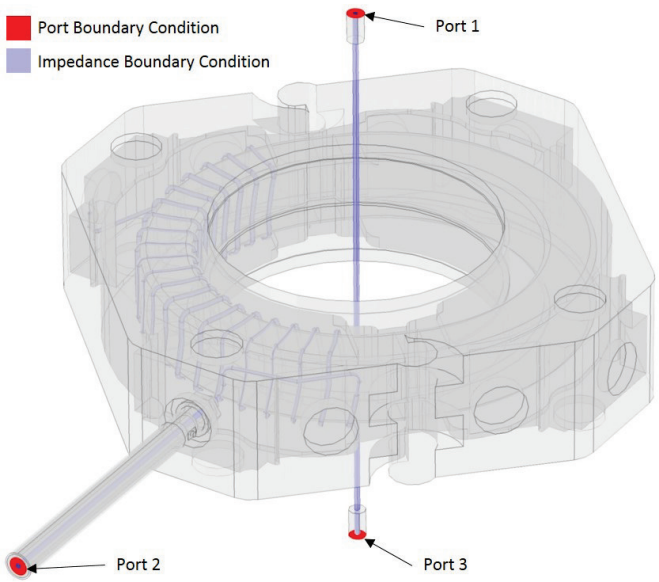

Fig. 4. Port and impedance boundary conditions. Energy enters the model through Port 1 and exits through Ports 2 and 3.

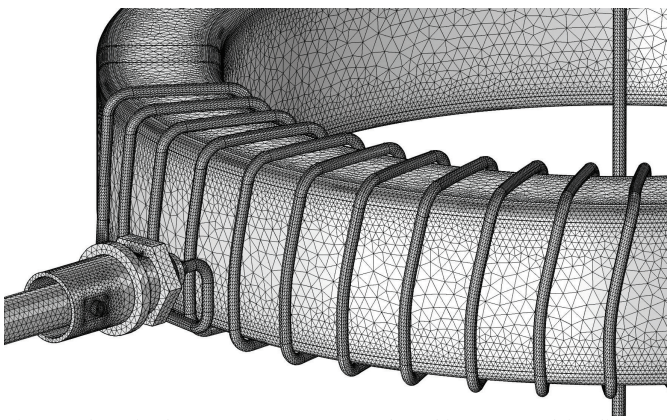

Fig. 5. Discretized HFCT geometry. Manual meshing was used for different parts of the model to improve element quality.

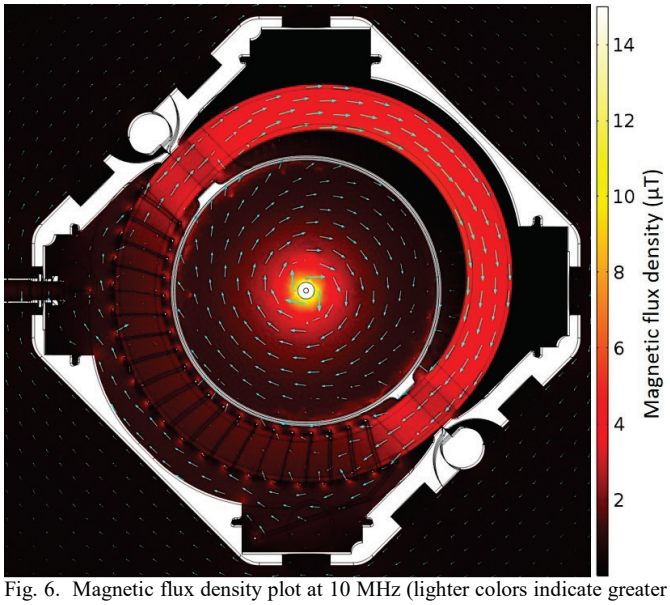

Fig. 6. Magnetic flux density plot at 10 MHz (lighter colors indicate greater magnitude). The magnetic field lines are visualized as an arrow plot.

A. *Effect of Winding Turns*

As with any other current transformer, the current output of the sensor (I_S) is inversely proportional to the number of sensor winding turns (N_S):

$$I_S = I_P\left(\frac{N_P}{N_S}\right) \tag{11}$$

where I_P is the current in the center conductor and $N_P = 1$. Consequently, the number of winding turns is one of the parameters that greatly affects the performance of the sensor.

Fig. 7 shows how the simulated frequency response of the HFCT changes as the number of winding turns varies. The turns were spread over the same arc length, maintaining the winding termination points identical. As expected, sensitivity increases as the number of turns decreases. At the same time the bandwidth of the sensor increases. A reduced number of turns widens the effective operating frequency range of the sensor (between -3 dB points) and extends it towards higher frequencies. Conversely, increasing the number of turns allows the sensor to operate at lower frequencies, but with reduced sensitivity.

Another interesting observation is the appearance of a gain dip in the response of the HFCT which effectively determines the highest operating frequency of the sensor. The gain dip is present in all three responses of Fig. 7. However, as the number of winding turns increases the gain dip appears at a lower frequency. For the model with 25 turns the dip appears at 40 MHz. The effect can be attributed to the increased interturn capacitance introduced by the additional turns.

B. *Effect of Spacer Thickness*

The introduction of gaps in the magnetic core of transformers is a technique frequently used to increase the saturation limit and allow the transformer to operate at higher current levels. The gap increases the reluctance of the core which in turn reduces the amount of flux flowing for a given current level. The gap can consist of air or any other material immune to saturation (nylon in the case of the HFCT). Although essential for avoiding saturation, adding a gap in a transformer core produces a reduction in the effective core permeability.

Fig. 8 shows how the frequency response of a HFCT sensor with 20 winding turns is affected by changes in spacer thickness. Predictably, the sensor sensitivity drops as the thickness of the spacer increases. This drop however is not constant across the frequency range and hence the bandwidth of the sensor changes. Although the high frequency cut-off point remains almost unaffected as the spacer thickness increases (approximately 42 MHz), the low frequency cut-off point shifts to a higher frequency. Therefore, the HFCT with a thinner spacer (smaller core gap) has a wider bandwidth and higher low frequency sensitivity.

C. *Effect of Aperture Size*

The aperture for the HFCT being examined in this study is a slit in the metallic casing of the sensor (Fig. 9). The aperture allows for better coupling between the current carrying wire and the winding, as well as preventing the casing from

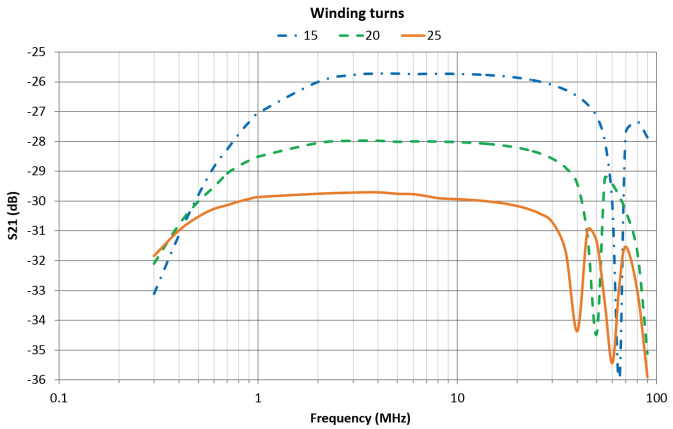

Fig. 7. Effect of the number of winding turns on the frequency response of the HFCT sensor.

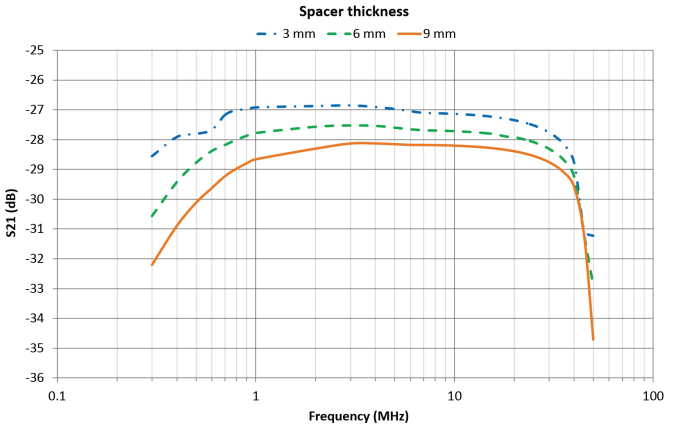

Fig. 8. Effect of spacer thickness on the frequency response of the HFCT sensor.

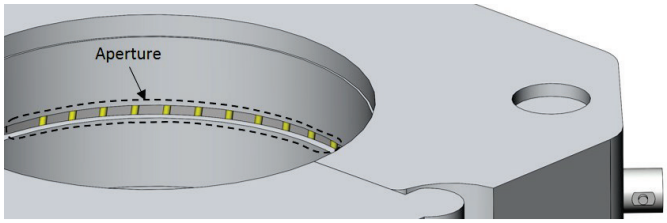

Fig. 9. HFCT aperture. It allows for better coupling between the current carrying wire and the winding.

forming a short-circuited turn around the core and reducing sensitivity.

Fig. 10 shows how the size of the aperture impacts on the response of a sensor with 20 winding turns. Increasing the aperture yields minor improvements to the low frequency sensitivity. Also, the bandwidth of the sensor does not change significantly. Increasing the aperture size above 1 mm though, causes a dip in gain to appear around 42 MHz for this specific HFCT model.

D. *Effect of Core Material*

As demonstrated earlier, the core plays a vital role in the operation of the HFCT. Due to the varying permeability of the ferrite over the frequency range of interest, it is difficult to determine how the core material influences the performance of the sensor with circuit based models. Examining the effect of the core material is straightforward when using FEA since different materials can be simulated by changing the material properties of the core domain. This allows for all geometric parameters to remain identical ensuring that the calculated effect is only attributable to the core material.

Fig. 11 shows a comparison between a HFCT model with a ferrite core and a HFCT model with an air core. The benefit of the ferrite is much more pronounced at the low frequency end of the response. For frequencies above 10 MHz the winding on its own is capable of raising the sensitivity to acceptable levels. Interestingly, while the permeability of the ferrite is dramatically reduced after 10 MHz (Fig. 3), the HFCT with the ferrite core still holds a significant advantage in sensitivity over its air-core counterpart up to 40 MHz. This indicates that the ferrite is still more effective in guiding the magnetic flux

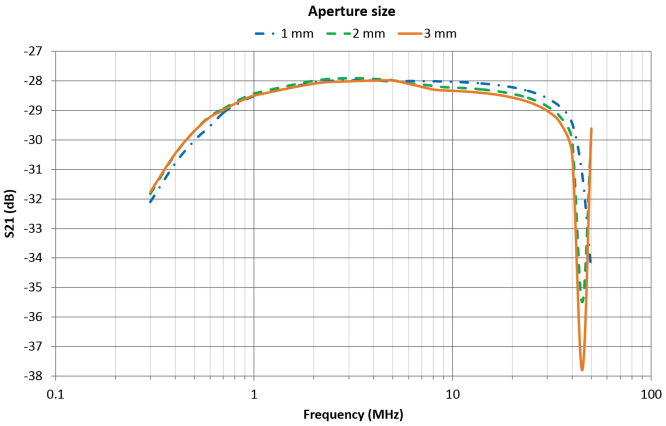

Fig. 10. Effect of aperture size on the frequency response of the HFCT sensor.

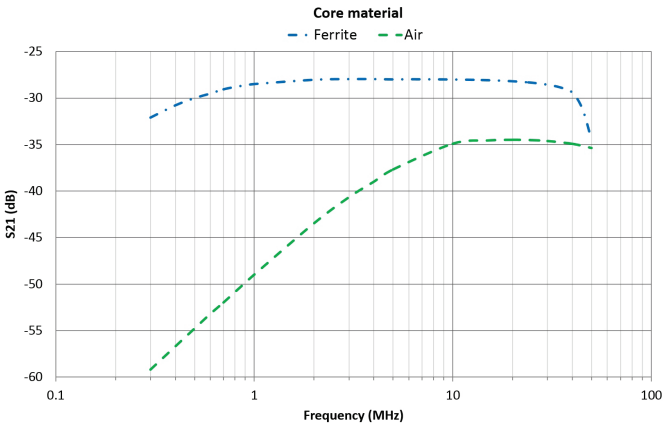

Fig. 11. Effect of core material on the frequency response of the HFCT sensor.

lines around the core than air despite the low permeability at higher frequencies. The effect can be attributed to the higher permittivity of the ferrite core which enhances the electric field in the vicinity of the winding and allows for more effective capacitive coupling of high frequency components from the primary to the secondary of the HFCT.

IV. Testing

A. *Test Setup*

Fig. 12 shows the test arrangement used to measure the forward gain of the HFCT (S_{21}-parameter). As with the simulation, the HFCT is placed inside a metal box which can accept an input from a signal generator via a coaxial cable. The shield of the cable was terminated on the box and its center conductor continued through the box and the middle of the HFCT. The output of the HFCT was connected to an oscilloscope via another coaxial cable. The HFCT sits on an insulating spacer so it does not come in contact with the walls of the box.

The S_{21}-parameter can be measured from the ratio of output to input voltage over a known impedance. The impedance is chosen to be 50 Ω since the HFCT in service will be connected to coaxial signal cables with 50 Ω characteristic impedance. Hence, the gain in dB can be calculated as:

$$S_{21} = 20\log\left(\frac{V_{out}}{V_{in}}\right) \tag{12}$$

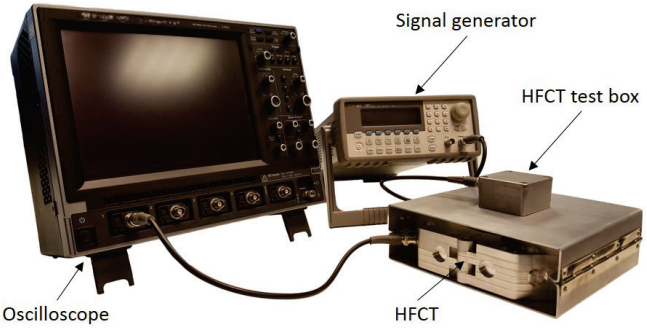

Fig. 12. HFCT test arrangement. The HFCT test box 'converts' the HFCT to a two-port device allowing the measurement of S-parameters.

The sensitivity, R_x, can be derived from S_{21} as follows:

$$R_x = 50 \cdot 10^{\left(S_{21}/20\right)} \quad (V/A) \tag{13}$$

B. Test Results and Comparison with Simulation

A prototype of the HFCT sensor was constructed and tested with the arrangement of Fig. 12. The prototype incorporated a 20 turn winding on a ferrite core, 9 mm spacers and a 1 mm wide aperture. A comparison between the measured and simulated S_{21}-parameters over the frequency range of 0.3 – 50 MHz is shown in Fig. 13.

The characteristics of the measured frequency response are quite similar to those of the frequency response computed by the simulation. The simulated S_{21} curve is slightly higher across the entire frequency range but the difference is relatively small, approximately 1 dB on average. The computed operating frequency range (-3 dB) is 0.38 MHz to 45 MHz while the measured range is 0.43 MHz to 33 MHz. Of particular importance for PD detection is the low frequency cut-off point of the sensor where the simulation and measurements differ by only 0.05 MHz. Possible reasons for the difference between the computed and measured values are discussed in the following section.

V. Discussion

After tackling the various challenges presented while undertaking this study, the following recommendations have been drawn which can be applied to similar studies:

1. Modelling the HFCT requires the use of more than one FEA software module to simulate its behavior over the entire operating frequency range. Inevitably, slightly different discretization and boundary conditions need to be used when switching from one FEA module to the other. It is important to verify that the behavior of the model is not affected by using a different module for the simulation. One of the checks performed for this study was to run all the simulations at 5 MHz using both the AC/DC and RF modules. The S_{21} for all cases was found to be consistently higher with the AC/DC module but the difference never exceeded 0.5 dB (e.g. for the 3 mm aperture in Fig. 10).
2. When using the *Magnetic Fields* interface, the use of a small non-zero conductivity for air might be required to avoid creating a singular stiffness matrix which would result in non-convergence or increased computation time [16]. Values up to one S/m can be used without affecting the physics of most simulations. However, for the simulations detailed in this study, using a conductivity for air equal to one S/m resulted in a significant reduction to the computed S_{21} parameter (up to 6 dB at 5 MHz). Before using a non-zero conductivity for air it is advised to investigate the effects different values will have on the solution and the time required for the computation.
3. Despite the simulation being designed to resemble the test arrangement, some approximations had to be employed, such as the *IBC*, to decrease the amount of computational resources required. For the same reason, parts of the test arrangement were not included in the simulation (the full-length coaxial cables), or were considered to be ideal i.e. without losses (the metal box). Furthermore, the tolerance of material properties is not taken into account for the simulation. For example, the ferrite has a permeability tolerance of ± 20% according to the manufacturer, which may significantly affect the results. The computed results, albeit very close, are not identical to the measured values and the aforementioned factors could contribute to the discrepancy.

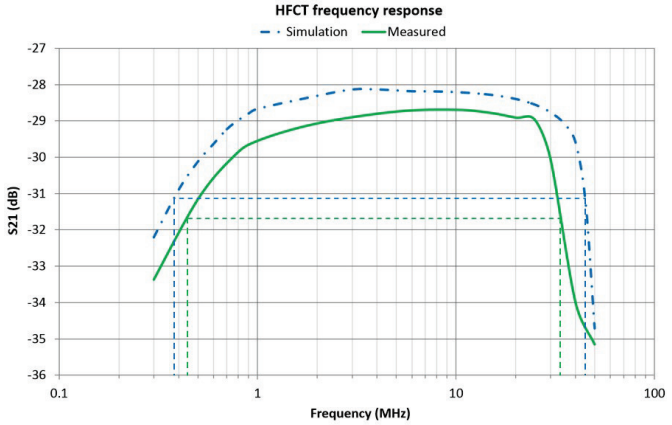

Fig. 13. Comparison between the computed and measured S_{21}-parameter. The operating frequency range in either case is indicated with dashed lines.

By examining the performance of the HFCT using FEA the following observations were made that can be used when designing and optimizing such sensors:

1. Decreasing the number of winding turns will increase the sensitivity of the sensor. Unfortunately, by doing so the effective operating range of the sensor is pushed towards higher frequencies. This is an undesirable characteristic when it comes to detecting PD, especially when the sensor is used for remote monitoring, since the high-frequency discharge pulse signals are attenuated before they reach the sensor.
2. Having a gapped core is mandatory for many HFCT applications in order to avoid magnetic core saturation in the presence of high currents. However, increasing the size of the gap reduces the bandwidth and the low frequency sensitivity of the sensor. The latter is particularly important for PD detection.
3. Certain combinations of geometric and material parameters can introduce a dip in the sensor gain. If the frequency steps at which the frequency response is simulated or measured are too broad, the dip might not be detected, causing an inaccurate characterization of the HFCT.
4. Although the sensor is a High Frequency Current Transformer, the ferrite core does not necessarily need to have high permeability at the higher end of the operating frequency range. This is because the contribution of the winding to the sensitivity becomes more significant as the frequency increases. By choosing an appropriate combination of ferrite and number of winding turns the sensor could be fine-tuned to have specific response characteristics.

VI. Conclusion

The benefits of using FEA to optimize the performance of a HFCT sensor are numerous. Compared to other methods, the capability of the FEA software to import accurate 3D models of the sensor components helps to avoid over-simplification of the geometry and therefore produce more accurate results. The effect of specific material properties or part dimensions on the performance of the sensor can be examined in isolation since they can be easily changed in the virtual domain. Finally, the development of new sensors can be greatly accelerated as the expensive and time consuming construction of multiple prototypes can be avoided.

A set of recommendations is given in the Discussion for setting up similar simulations and designing HFCT sensors.

Acknowledgment

The authors would like to thank Mr. Hubert Schlapp for his contribution in designing the HFCT test box and his advice on how to construct and test HFCT sensors.

References

[1] G. C. Stone, "Partial discharge diagnostics and electrical equipment insulation condition assessment," *IEEE Transactions on Dielectrics and Electrical Insulation,* vol. 12, pp. 891-904, 2005.

[2] R. Giussani, L. Renforth, M. Seltzer-Grant, and C. Zachariades, "A holistic combined electrical and mechanical condition monitoring technique for oil and gas high voltage rotating machines," *Electrical Insulation Conference (EIC), 2015 IEEE*, 2015, pp. 283-287.

[3] F. P. Mohamed, W. H. Siew, J. J. Soraghan, S. M. Strachan, and J. McWilliam, "The use of power frequency current transformers as partial discharge sensors for underground cables," *Dielectrics and Electrical Insulation, IEEE Transactions on,* vol. 20, pp. 814-824, 2013.

[4] L. A. Renforth, P. S. Hamer, D. Clark, S. Goodfellow, and R. Tower, "Continuous Remote Online Partial Discharge Monitoring of HV Ex/ATEX Motors in the Oil and Gas Industry," *Industry Applications, IEEE Transactions on,* vol. 51, pp. 1326-1332, 2015.

[5] M. Shafiq, L. Kutt, M. Lehtonen, T. Nieminen, and M. Hashmi, "Parameters Identification and Modeling of High-Frequency Current Transducer for Partial Discharge Measurements," *Sensors Journal, IEEE,* vol. 13, pp. 1081-1091, 2013.

[6] P. Poulichet, F. Costa, and E. Laboure, "High-frequency modeling of a current transformer by finite-element simulation," *IEEE Transactions on Magnetics,* vol. 39, pp. 998-1007, 2003.

[7] C. E. C. Quispe, "HF characterization and modeling of magnetic materials for the passive components used in EMI filters," Génie Électrique, Ecole Doctorale des Sciences Pour l'Ingénieur, Université Lille 1 - Sciences et Technologies, 2013.

[8] F. Fiorillo, C. Beatrice, O. Bottauscio, and E. Carmi, "Eddy-Current Losses in Mn-Zn Ferrites," *Magnetics, IEEE Transactions on,* vol. 50, pp. 1-9, 2014.

[9] W. Frei. (2013). *Computational Electromagnetics Modeling, Which Module to Use?* Available: http://www.comsol.com/blogs/computational-electromagnetics-modeling-which-module-to-use/

[10] W. Frei. (2015). *Modeling Metallic Objects in Wave Electromagnetics Problems*. Available: http://www.comsol.com/blogs/modeling-metallic-objects-in-wave-electromagnetics-problems/

[11] W. H. Hayt and J. A. Buck, *Engineering Electromagnetics*, 8th ed. New York: McGraw-Hill, 2012.

[12] W. Frei. (2015). *Modeling of Materials in Wave Electromagnetics Problems*. Available: http://www.comsol.com/blogs/modeling-of-materials-in-wave-electromagnetics-problems/

[13] S. Marburg, "Six Boundary Elements per Wavelength: Is That Enough?," *Journal of Computational Acoustics,* vol. 10, 2002.

[14] R. Lee and A. C. Cangellaris, "A study of discretization error in the finite element approximation of wave solutions," *Antennas and Propagation, IEEE Transactions on,* vol. 40, pp. 542-549, 1992.

[15] W. Frei. (2013). *Meshing Considerations for Linear Static Problems*. Available: http://www.uk.comsol.com/blogs/meshing-considerations-linear-static-problems/

[16] COMSOL Inc., *Single-turn and multi-turn coil domains in 3D*, 2012.

Christos Zachariades was born in Athens, Greece, in 1984. He received the BEng (Hons) in electrical and electronic engineering, in 2009, the MSc in electrical power systems engineering, in 2010, and the PhD in electrical and electronic engineering, in 2014, from the University of Manchester, UK.

Since 2014, he has been working as a Development Engineer and Knowledge Transfer Partnership Associate with HVPD Ltd, UK, and the University of Manchester.

Dr. Zachariades is a member of the Institution of Engineering and Technology (IET) and a member of the Cyprus Scientific and Technical Chamber (ETEK).

Roger Shuttleworth (M'07) was born in the UK and completed his BSc and PhD degrees in electrical and electronic engineering at The University of Manchester, UK.

He worked for a year at GEC Traction before joining the University as a lecturer in the Power Systems Research group and later the Power Conversion Research group. He has around 100 papers and patents and is Director for the Power Electronics, Machines and Drives MSc course.

His main research activities are in the areas of Power Electronics, Energy Control and Conversion, and Energy Harvesting.

Riccardo Giussani (StM'10, M'13) was born in Legnano, Italy, in 1978. He received the EngD in electrical engineering from Politecnico di Milano, Italy, and the PhD in electrical and electronic engineering from the University of Manchester, UK, in 2015.

Since 2013, he has been working as a Senior Development Engineer at HVPD Ltd, UK.

Dr. Giussani is a member of Institution of Engineering and Technology (IET) and the IEEE Dielectrics and Electrical Insulation Society (DEIS).

Ross MacKinlay was born in the UK, in 1951. He received the BA (Hons) in physics from Lancaster University, UK, and the DPhill in physics from Keble College Oxford, UK.

He was Managing director of High Voltage Solutions, UK, from 1998 to 2008, and Technical director of HVPD Ltd, UK, until 2016, when he retired. He has developed many new methods in the detection of Partial Discharges (VLF, on-line detection, PD mapping, etc.).

Dr. Mackinlay is a member of the Institution of Engineering and Technology (IET).